Passive multichannel analysis of surface waves using 1D and 2D receiver arrays

Sarah L. Morton[1], Julian Ivanov[1], Shelby L. Peterie[1], Richard D. Miller[1], and Amanda J. Livers-Douglas[2]

ABSTRACT

We use the seismic multichannel analysis of surface waves (MASW) method, which originally used active sources (i.e., controlled by users), to present a new alternative technique for surface-wave analysis of passive data (i.e., seismic sources not controlled by users). Our passive MASW technique uses two types of receiver arrays, 1D and 2D, for two different purposes. The 2D square array is used for assessing the number and directionality of passive seismic sources to help identify optimal time window(s) when such sources are of sufficient quality and aligned with the 1D receiver spread. Then, these time windows are used to selectively extract passive seismic data recorded by the 1D receiver spread for subsequent MASW analysis. In such a manner, this hybrid 1D–2D passive MASW approach can approximate the higher quality advantages of the active MASW method. This technique is successfully applied at a test site in southcentral Kansas taking advantage of train energy as the passive sources monitoring and assessing the potential development of vertically migrating voids that could endanger groundwater and infrastructure. The 1D–2D passive MASW method has proven beneficial for optimizing passive-data dispersion patterns and accurately assessing relative velocities for investigations with reduced labor costs and minimal added processing time and can be considered as a contribution to the surface-wave analysis tools.

INTRODUCTION

Surface-wave methods are increasingly being used to image the subsurface and evaluate changes in its mechanical properties and in situ processes. The active multichannel analysis of surface waves (MASW) method (Song et al., 1989; Park et al., 1998; Miller et al., 1999; Xia et al., 1999) has demonstrated success imaging the upper 30 m for applications to map bedrock (Miller et al., 1999), detect faults and voids (Ivanov et al., 2006; Xu and Butt, 2006; Karastathis et al., 2007), image karst features (Dobecki and Upchurch, 2006; Parker and Hawman, 2012; Morton et al., 2020), and other applications. However, the depth of investigation depends on the longest available coherent wavelength (usually related to the lowest frequency), which in turn depends on the output of the seismic source, as well as the geologic environment (e.g., maximum velocities), receiver specifications, and recording array geometry (Sheriff and Geldart, 1995). Therefore, the seismic source used during data acquisition must be able to generate and transfer longer wavelengths for deeper investigations. Most active sources, such as mechanical weight drops or sledgehammers, are bandwidth-limited due to their physical limitations. To overcome this, passive surface-wave methods have been used to successfully achieve depths from tens to hundreds of meters below the ground surface (Delgado et al., 2000a; Louie, 2001). These passive methods use ambient noise sources that are not controlled by the survey operator; these passive sources may include ocean tides, earthquakes, or local traffic that have low-frequency energy characteristics (Delgado et al., 2000b; Asten et al., 2004; Beroya et al., 2009).

More recently, there has been a growing interest in the application of ambient-noise data interpretation at the engineering and environmental scale (e.g., upper 100 m) for problems that require shallow site characterization (Delgado et al., 2000a; Beroya et al.,

2009; Rosenblad and Goetz, 2010). These surveys typically deploy 3C seismometers as either single-station (Nakamura, 1989; Bonnefoy-Claudet et al., 2006; Cornou et al., 2011) or 2D-shaped arrays such as circles or triangles to record surface-wave dispersion information (Henstridge, 1979; Asten, 2006; Bonnefoy-Claudet et al., 2006; Di Giulio et al., 2006). Park and Miller (2008) demonstrate that these 2D passive arrays can optimally image an accurate dispersion trend. The shape and size of passive arrays are often limited by the availability of space; single-station or cross-shaped arrays are more commonly used in urban settings given the higher density of infrastructure (Kind et al., 2004; Park and Miller, 2005; Claprood and Asten, 2007).

Some of the current passive surface-wave data processing methods include spatial autocorrelation (SPAC) (Aki, 1957; Chavez-Garcia et al., 2006; Luo et al., 2016; Asten and Hayashi, 2018), frequency-wavenumber (Capon, 1969; Socco and Boiero, 2008; Cheng et al., 2017), horizontal-to-vertical spectral ratio (HVSR) (Nogoshi and Igarashi, 1970, 1971; Nakamura, 1989; Carniel et al., 2008; Dal Moro, 2015; Molnar et al., 2018; Akkaya and Özvan, 2019), and refraction microtremor methods (Louie, 2001; Rosenblad and Li, 2009; Cox and Beekman, 2011; Silahtar et al., 2020). Detailed summaries and comparisons of each method with corresponding guidelines of practice have been compiled by Wathelet et al. (2008), Garofalo et al. (2016), and Foti et al. (2018). Other passive surface-wave methods using 1C array configurations have been developed as extensions of the conventional MASW method, including passive roadside (Park and Miller, 2008), hybrids of SPAC (Kita et al., 2011; Hayashi et al., 2015; Moon et al., 2017; Asten and Hayashi., 2018), and crosscorrelation algorithms (Cheng et al., 2015, 2016; Le Feuvre et al., 2015; Nakata, 2016; Zhang et al., 2019).

Seismic interferometry has gained popularity over the past 10 years because it can be simplified into two steps: Crosscorrelate two signal pairs and stack the result (Schuster, 2001, 2009; Curtis et al., 2006; Cheng et al., 2016; Zhang et al., 2019). This method assumes a diffuse wavefield in which incoming source energy has equal amplitude from all directions (Curtis et al., 2006; Schuster, 2009); an assumption that becomes invalid in the characteristically 2D near-surface environment (Snieder, 2004; Wapenaar et al., 2010). Therefore, S-wave velocities will be inaccurately estimated unless the receiver spread is in line with the direction of the source energy (Zhang et al., 2019) or higher mode surface-wave information is available and can be incorporated into the inversion scheme (Halliday and Curtis, 2008). Other studies have also noted a loss in low-frequency signal using seismic interferometry due to near-field effects, which can further reduce the reliability of velocity estimation (Cheng et al., 2015; Zhang et al., 2019).

Two-dimensional arrays, such as circles and triangles, are considered optimal for use with surveys that record multiple multidirectional passive sources (Rost and Thomas, 2002). However, these shaped arrays can be difficult to implement and operate (labor consuming) and difficult to roll across multiple locations. Linear arrays are the most efficient to operate (including streamers) and are most accurate when aligned with a source (i.e., inline wave propagation). Within the active MASW processing scheme, it is assumed that active-source energy propagates inline or parallel to the receiver spread (Park and Miller, 2008). However, passive source energy may propagate in line with or at an oblique angle to the linear receiver spread. When the seismic source is within one wavelength of the receiver spread (i.e., short-source offset), recorded surface-wave energy becomes more susceptible to near-field effects caused by offline wave propagations (Foti et al., 2018). Phase velocities will subsequently be underestimated at low frequencies due to these near-field effects (Bodet et al., 2009; Ivanov et al., 2011). S-wave velocities also can be overestimated if oblique or off-angle source energies are inadvertently incorporated into analysis without accounting for the incident angle (Park and Miller, 2008); overestimated velocity is referred to as apparent velocity.

In urban areas, various studies have used local traffic as passive surface-wave energy sources (Park and Miller, 2008; Zhao and Rector, 2010; Liu et al., 2014; Zhang et al., 2019). The passive roadside MASW method (Park and Miller, 2008) uses local vehicle traffic as passive seismic source energy to retrieve MASW S-wave velocity (V_S) sections from linear receiver spreads. This azimuthal scanning method (Park et al., 2004; Park, 2008) considers inline, offline, and offline cylindrical wave energies for dispersion analysis because the receiver spread is along and parallel to a road. However, S-wave velocity overestimation may still occur due to the presence of multiple multidirectional sources mentioned earlier.

In this paper, we present the 1D–2D passive MASW method: an optimized solution that incorporates the advantages of 1D and 2D arrays using optimal inline sources and avoiding interference from non-inline wave energy. We used an extended 1D fixed receiver spread to record remote passive sources (e.g., from distant passing trains) that are aligned with the linear array. In addition to the linear arrays, we simultaneously acquired a 2D square grid array for determining the azimuth of incoming passive source energy for optimal alignments (Park et al., 2007). With our novel approach, the 2D grid is not used for the purpose of the conventional MASW analysis but for passive-source quality control and assessment of orientation relative to linear arrays. Earlier efforts (Leitner et al., 2011, 2012) demonstrated that linear receiver spreads extracted from a 2D grid provided high-quality dispersion-curve images compared with those generated using the entire 2D grid. These observations encouraged the development of the 1D–2D passive MASW method using 1D linear receiver spreads. In such a manner, linear-array data that have optimal sources (e.g., locations aligned with the linear arrays, sufficient energy amplitudes at low frequencies, and no simultaneous obliquely oriented source energy) can be selected and used for further MASW analysis without rotation for true velocity estimates. Dispersion-curve imaging using passive-source linear-array data can be accomplished using the conventional active-source algorithms (Park et al., 1998) as well as other signal-to-noise ratio (S/N) enhancement tools (Park et al., 2002; Luo et al., 2008a, 2008b; Ivanov et al., 2017b; Morton et al., 2019) to produce high-amplitude surface-wave signatures. Furthermore, multiple shorter optimized-length subspreads can be extracted and analyzed with the MASW method to obtain numerous 1D V_S sections that can be integrated into a final MASW V_S section.

Field data examples are presented to demonstrate the effectiveness of this method for imaging the upper 60–80 m at a test site in southcentral Kansas monitoring velocity variations in bedrock overlying salt dissolution-mined voids near wells. The development of this method was motivated by a seismic investigation (Miller et al., 2009; Sloan et al., 2009) that was unable to measure S-wave velocity at depths greater than 10–19 m using the active MASW method in the same karst environment.

1D–2D PASSIVE MASW METHOD

Unlike omnidirectional passive seismic methods, this passive MASW method using 1D and 2D receiver arrays uses only seismic

sources that propagate along a linear and inline path similar to active seismic sources advancing along the geophone array. Although the source itself cannot be controlled in terms of strength and distance, the direction of the source relative to the receiver lines can be estimated from a 2D grid array and incorporated into data processing. However, it may not always be feasible to deploy a 2D array that covers a test site in its entirety due to the size of a survey area or limited equipment allowances. Instead, it has proven most effective to deploy a single 2D array at a fixed location central to multiple 1D receiver spreads with a size defined by the sensitivity to the longest wavelength expected. Such an approach can minimize field labor, time, and data processing and contribute to using selective, higher quality data and thus final results.

The 1D–2D passive MASW method can be summarized in five steps: (1) Collect passive seismic data simultaneously using one or more 1D and a 2D receiver arrays, (2) select an optimal source record using dispersion-curve images from 1D receiver spreads and frequency versus azimuth angle images (i.e., frequency-azimuth plots) from the 2D array, (3) estimate shorter optimal spread size that meets desired project specifications (e.g., preserving lowest frequencies for maximum depth analysis) and extract as many possible short-spread records with spread midstations that simulate roll-along data acquisition, (4) create dispersion-curve images from each roll-along spread segment and pick dispersion curves, and (5) invert those picked curves for 1D V_S sections that are combined into quasi-2D V_S sections (henceforth referred to as MASW V_S sections). Details pertaining to these steps are discussed in a later section. With the exception of steps 2 and 3, this procedure mimics the active MASW method described earlier (Park et al., 1998; Miller et al., 1999; Xia et al., 1999).

Great emphasis is given to source record selection, which is one of the core differences between the passive and active methods described here. Although many ambient noise methods combine all three components of the seismic wave, this method only considered the vertical component for Rayleigh-wave velocity analysis. Although the success of all dispersion-curve imaging and interpretation is largely dependent on source signal quality, this specific passive method relies on inline, low-frequency surface-wave signals from sources at least 1–2 km from the receiver spread. These signals are susceptible to varying degrees of overestimations, where unwanted, dominating offline ambient noise is recorded in the data. For the purpose of this work, an ideal source signal has a coherent seismic energy spectrum from 4 to 20 Hz that is concentrated within a single azimuth angle coinciding with the orientation of the fixed linear array. Details pertaining to azimuth-frequency imaging and dispersion-curve processing are described in the following subsections using passive data from a well-documented test site in south-central Kansas, USA.

Source record detection

The surface-wave azimuth image is generated using a 2D receiver grid composed of four nested square arrays with 131 vertical geophones at 5 m receiver spacing (Figure 1); the symmetric square shape is used instead of a circle, triangle, or cross for positioning convenience during survey deployment. The 2D array also limits azimuth bias of the recorded signal by eliminating multidirectional source environments from 1D array processing and to help identify source records with single sources from a preferred incoming direction (Park and Miller, 2008). Similar to the dispersion-curve

imaging, which stacks phase-velocity information at a given frequency increment (Park et al., 1998), frequency-azimuth plots are produced by stacking azimuth information at degree-angle increments for energy spanning a specified frequency range (Park et al., 2004). Recorded wavefronts are considered inline plane-wave propagation rather than spherical wave propagation because they originate from distances two times greater than the radius of the recording 2D array (Park, 2008).

Given a 2D array, incoming surface-wave energy, $E_{2D}(\omega, c, \theta)$, is dependent on three parameters including frequency ω, scanning phase velocity c, and azimuth θ. This energy is estimated using equation 1 from Park et al. (2004), where a phase shift φ_i is applied to the Fourier transform $R_i(\omega)$ of ith trace along the x- and y-axes of the 2D array,

$$E_{2D}(\omega, c, \theta) = \left| \sum_{ix=1}^{NX} e^{j\varphi_{ix}} R_{ix}(\omega) + \sum_{iy=1}^{NY} e^{j\varphi_{iy}} R_{iy}(\omega) \right|. \quad (1)$$

Energy is the absolute value of the summed NX and NY phase-shifted traces. The estimated energy peaks are projected into frequency-azimuth (ω-θ) space using the grid receiver coordinate system configured into 2D concentric square arrays using GPS-assigned positions during acquisition (Figure 1). By performing these steps, linear trends will be mapped on frequency-azimuth plots (Figure 2) with respect to the frequency and azimuth (Park et al., 2008). The azimuth angle is measured in degrees counterclockwise from east (0°) such that surface waves propagating from east to west will plot across 180° (Figure 2a) and surface waves propagating from west to east will plot along 0° (Figure 2b). Therefore, trends illustrate the incoming direction or angle at which seismic energy was recorded traveling through the 2D grid array.
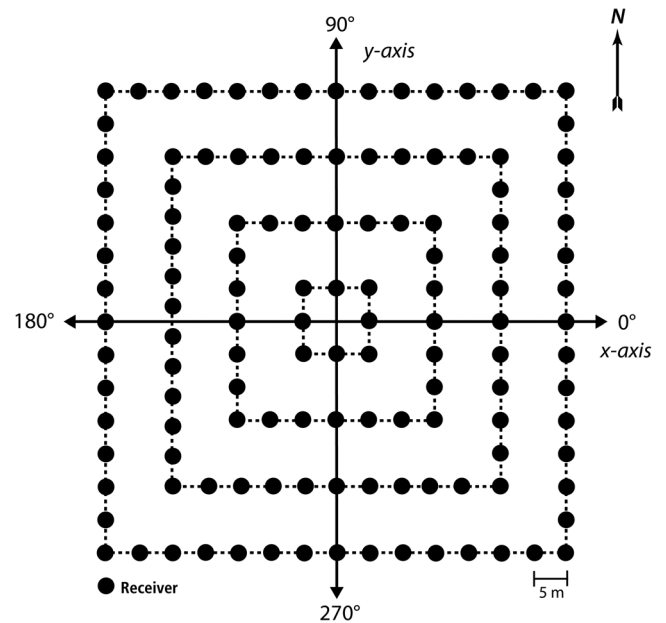

Figure 1. Four nested square arrays were deployed using 131 vertical geophones at 5 m spacing to construct the 2D grid to analyze source azimuth information.

For a given frequency, multiple energy peaks may exist at different phase velocities and azimuths if multiple surface-wave modes and energy sources are present. Dispersion-curve images are generated using energy, $E'_{2D}(\omega, c)$, estimated with equation 2 (Park et al., 2004):

$$E'_{2D}(\omega, c) = \sum_{i=1}^{N_\theta} E_{2D}(\omega, c, \theta_i). \tag{2}$$

All of the surface-wave energy is summed for N_θ azimuths based on the same scanning frequency and phase-velocity intervals from equation 1. These dispersion-curve images display constructively stacked surface-wave dispersion trends from all sources recorded in the c-θ space. All of the data were processed using *SurfSeis* and *KGS SeisUtilities*, proprietary software packages developed by the Kansas Geological Survey.

Source record selection

For this method, it is critical that an adequate source record (i.e., frequency-azimuth plot) is selected to produce a coherent dispersion-curve trend. An adequate source record includes linear frequency amplitude information that spans the desired frequency range (e.g., 1–20 Hz) and is limited to a narrow range of angles relative to the orientation of the 1D receiver spread (Figure 3a). Source records that do not meet these guidelines have no dominant azimuth, and the frequency-azimuth plots appear as amplitude anomalies focused in small or discontinuous frequency bands at various angles (Figure 3b). On the frequency-azimuth plots (Figure 3), fundamental-mode energy cannot be differentiated from higher modes or other noise energy. Therefore, corresponding dispersion-curve images are generated to assess the overall quality

of surface-wave trends. For example, on a frequency-azimuth plot there may be high-amplitude energy imaged below 5 Hz, which would imply the potential for imaging dominant longer wavelengths. However, the corresponding dispersion-curve image may reveal that this high-amplitude energy is a combination of offline energy (i.e., seismic energy originating from sources propagating at an oblique angle relative to the linear array) and higher modes that are masking the fundamental-mode trend. It is preferred to select dispersion-curve images whose low-frequency energy exhibits well-defined wave separation to reduce mode misidentification and the need for slope filtering. The frequency-azimuth plot that meets the described criteria is selected as the source record for generating dispersion-curve images along that survey line.

Data are collected overnight for periods exceeding 12 h. These longer durations increase the opportunity to record seismic energy aligned with the fixed array's orientation in the field. If a single source file does not contain sufficient S/N of low-frequency surface-wave amplitudes, multiple source files with intermittent energy that otherwise meet the criteria for these source image files can be stacked to increase the S/N. It is important to note that only the dispersion-curve images are stacked, not the raw seismic records. Caution should be taken when stacking multiple frequency-azimuth plots to limit the variability of incoming energy and reduce aliasing. Then, spread tests are performed to determine the shortest spread length that will yield the highest possible lateral resolution without adversely affecting the fundamental-mode signature.

FIELD TEST EXAMPLES

At a test site in southcentral Kansas (Figure 4), surface-wave data were acquired to monitor changes in rock competency between the
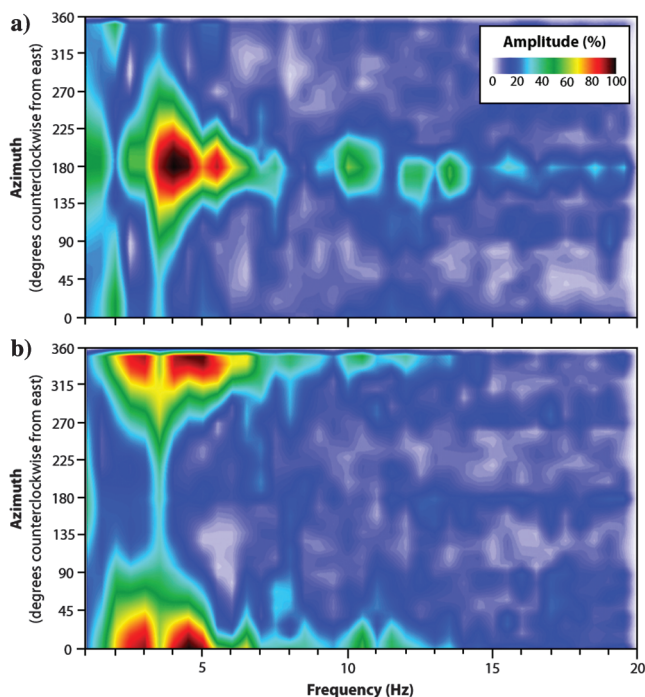

Figure 2. Frequency-azimuth plots where (a) surface waves propagating west to east are plotted across 180° and (b) surface waves propagating east to west are plotted across 0°.
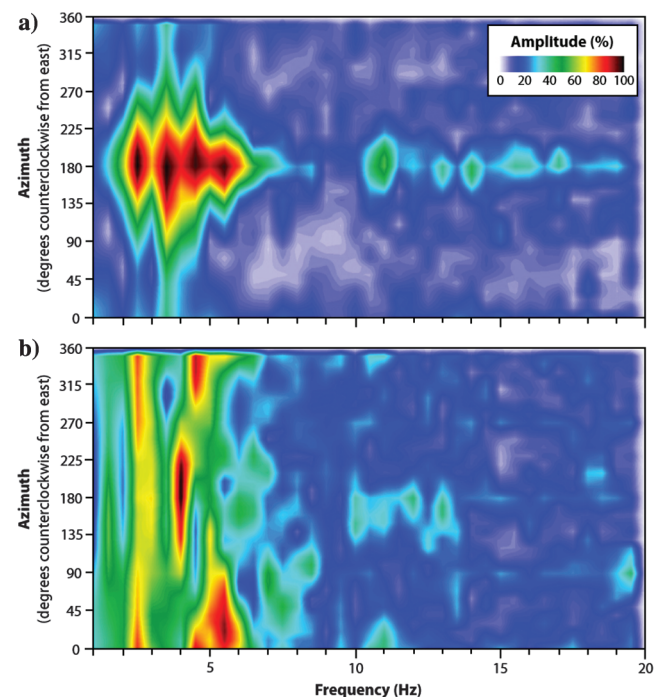

Figure 3. Examples of frequency-azimuth plots with (a) high-quality linear signals from record 3480 and (b) poor-quality multidirectional signals from record 3455.

Ninnescah Shale bedrock surface (approximately 21 m below ground surface [BGS]) and basal contact of the Wellington Formation (approximately 250 m BGS) in relation to the presence of known dissolution-mined voids in the Hutchinson Salt Member of the Wellington Formation (Walters, 1978; Ivanov et al., 2013; Morton et al., 2020). These approximately 30 m diameter dissolution-mined voids are referred to as salt jugs for their jug-like shape. Dissolution-mining operations using methods (e.g., single-well, multiwell, room-and-pillar) susceptible to long-term void stability problems were common throughout the late 19th and early 20th centuries. During that time, these operations were much less regulated and lacked the engineering design that is common in today's practices and necessary to minimize void roof degradation and failure. Many well sites in this area remain susceptible to the vertical migration of these legacy voids and potential ground failure (Walters, 1978).

Because V_S is directly related to the shear modulus, or stiffness, MASW V_S sections from inverted surface-wave energy provide a measure of material strength. Therefore, anomalous areas of decreased or increased V_S correspond to areas of decreased stiffness (weakening) or increased stiffness (stress build up). With time-lapse surface-wave analysis, successful detection of these temporal velocity variations and associated failure potential or evidence of previous failure conditions provide early warnings that can allow action to minimize the impacts to infrastructure prior to sinkhole development (Morton et al., 2020). In addition, estimates of depth below the ground surface to halt the vertical migration of a void due to sufficient bulking can allow estimates of future ground stability.

Borehole logs report an average 21 m of alluvial materials and Pliocene-Pleistocene Equus beds at the surface above the bedrock, which is the Ninnescah Shale (Watney et al., 2003). The top of the Hutchinson Salt Member varies from 60 to 80 m depth; therefore, the depth of interest for this investigation is between 60 and 80 m.

Active versus passive source data comparison

In 2008, an active seismic investigation of the Hutchinson Salt Member was performed using S-wave seismic reflection and conventional MASW data acquisition (Figure 4) to determine whether known dissolution-mined voids below wells and the associated in situ stress conditions could be detected noninvasively (Miller et al., 2009; Sloan et al., 2009). However, 7.8 Hz was the lowest frequency ($f = v/\lambda$) achieved with the active MASW method on line 1 (Figure 5a). The minimum and maximum depths of investigation can be estimated from these data sets because the approximate depth of investigation for Rayleigh waves is equal to its wavelength (Richart et al., 1970) and the calculated depth of inverted S-wave velocities is half the wavelength (Rix and Leipski, 1991). Therefore, the longest available wavelength was only approximately 28 m ($\lambda_{max} = 217/7.8 = 27.8$ m), yielding a maximum depth of investigation of approximately 14 m ($z_{max} = 27.8/2 = 13.9$ m) and not penetrating the entire 21 m alluvial interval. Survey parameters for the active MASW survey included (144) 4.5 Hz vertical geophones deployed at 1.8 m (4 ft) intervals, a 6 m active-source offset, and a 42.67 m (140 ft) subspread extracted from the fixed receiver spread (Table 1). Although some lower frequencies were observed, the signal was attenuated between 5.5 and 7.0 Hz, limiting fundamental-mode interpretation within this frequency range (Figure 5a). Therefore, the 1D–2D passive MASW method was developed to instead use nearby passing trains (1–2 km away) as sources for lower frequency energy.

In 2017, a new MASW survey was designed to acquire passive seismic data along the same spatial location of the 2008 active
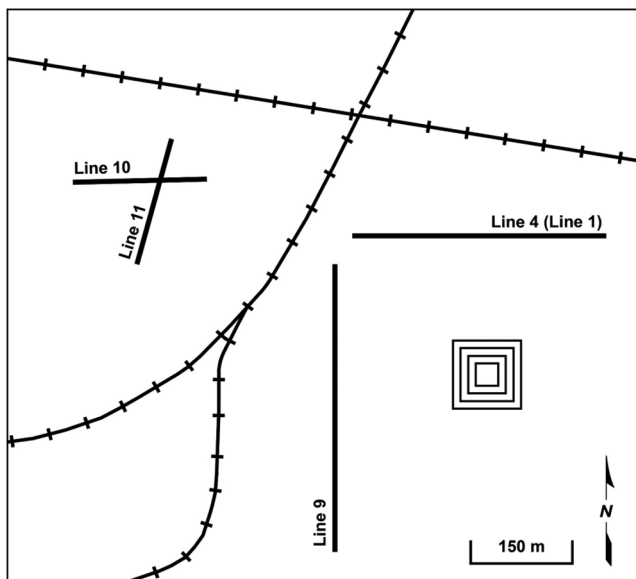

Figure 4. Field test site in southcentral Kansas where linear receiver spreads were deployed for active and passive seismic data acquisition. The 2008 active MASW study included line 1 and the 2017 passive MASW study included lines 4, 9, 10, and 11. The location of the 2D grid used for passive acquisition is illustrated as four concentric squares.
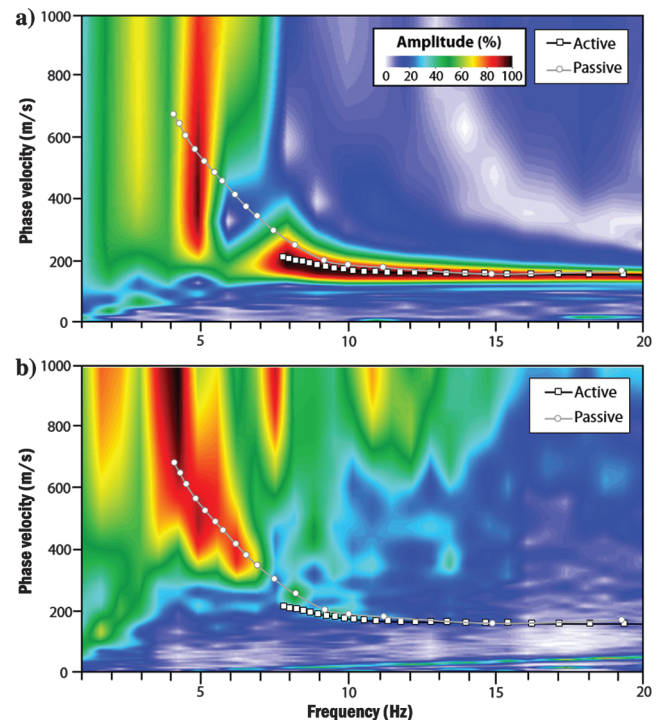

Figure 5. Dispersion-curve images from (a) the 2008 active survey along line 1 and (b) 2017 passive survey along line 4. The curve with the white squares represents picked active data set from 7.8 to 39.4 Hz though data shown only to 20 Hz; the curve with the white circles represents picked passive data set from 4.5 to 20.0 Hz for brevity.

MASW data set (Figure 4). Line 4 was deployed with a 180° survey line orientation relative to the east (Figure 1) and passive source energy generated by trains yielded high S/N, coherent fundamental-mode dispersion energy from 4.5 to 20.0 Hz (Figure 5b). Passive survey parameters for line 4 included (168) 4.5 Hz vertical geophones deployed at 3 m intervals and an optimal 84 m subspread extracted from a fixed 1D receiver spread (Table 1). To determine the direction of passive source energy relative to the linear receiver spread, a 2D square grid array was also deployed, which consisted of four concentric squares of 4.5 Hz vertical geophones spaced at 5 m intervals.

Fundamental-mode trends from the active (Figure 5a) and passive (Figure 5b) surveys are superimposed on dispersion-curve images in which both images have similar trends at frequencies greater than 9 Hz. Phase velocity did vary by an average of 11% between 7 and 10 Hz due to differences in dispersion-curve image resolution and receiver spread size between the active and passive data sets. The resulting MASW V_S sections for lines 1 and 4 from the active and passive studies, respectively, are shown in Figure 6. Inter-

pretation of dispersion curves from the 2008 active MASW data set was limited to frequencies >7 Hz (Figure 5a). The minimum and maximum wavelengths recorded were approximately 4 m ($\lambda_{min} = 156/39.4 = 3.8$ m) and 28 m ($\lambda_{max} = 217/7.8 = 27.8$ m) (Figure 5a), which correspond to 2–14 m inverted depths ($z_{min} = 3.8/2 = 1.9$ m; $z_{max} = 27.8/2 = 13.9$ m). The 1D–2D passive MASW method achieved greater penetration depths compared with the active method (Figure 6b). The velocity structure in Figure 6b is consistent with alluvial materials sampled from 0 to 21 m, the (weaker) Ninnescah Shale and the (firmer) Wellington Formation from 21 to 80 m, and the Hutchinson Salt Member below 80 m. The minimum and maximum wavelengths recorded were approximately 9 m ($\lambda_{min} = 172/19.3 = 8.9$ m) and 167 m ($\lambda_{max} = 684.6/4.1 = 166.9$ m) (Figure 5b), which correspond to 4.5–83.5 m inverted depths ($z_{min} = 8.9/2 = 4.45$ m; $z_{max} = 166.9/2 = 83.45$ m). Compared to the MASW V_S section from active data, the average velocity of the uppermost layer was within 10% of that estimated in the passive MASW V_S section. Based on this work, other recent passive MASW surveys conducted at this test site (Ivanov et al., 2013; Morton et al., 2020), and the consistency between the velocity structure and known material characteristics, this 1D–2D passive MASW method successfully imaged an average 77 m depth of investigation using passing trains as a passive seismic source. This average depth to the half-space layer is within range of the Wellington Shale-Hutchinson Salt Member boundary at a depth of 80 m that the active survey could not achieve.

180°, 90°, and 74° survey line orientations

The 2D grid consists of four concentric squares that are deployed using (131) 4.5 Hz vertical geophones at 5 m spacing. In addition to this 2D grid, several fixed linear arrays using 4.5 Hz vertical geophones at 3 m spacing are also deployed to monitor stress conditions surrounding other wells in this field area; total spread lengths vary from 200 to 250 m (Figure 4). These linear arrays are later decimated into shorter rolling spreads (e.g., 70–120 m) for dispersion-curve processing.

Energy from passing trains (i.e., 1–2 km away) has turned out to be the preferred ambient noise source at this site used to obtain long enough wavelengths to sufficiently image depths greater than 30 m rather than residential vehicle traffic or other sources. The arrival and incoming direction of each passing train were verified by the seismic survey operator based on calibrated observations such as train noise (e.g., train whistle or horn) and the seismograph's noise floor during overnight acquisition of seismic records. These calibrated observations were initially provided by field personnel to allow the survey operator to develop a qualitative method to estimate the incoming train distance. In the current approach, the survey operator takes similar observations into consideration during source record selection. Passive seismic data (Figure 7) are collected nearly continuously in consecutive 30 s records (2 ms sampling rate) throughout the night from the 1D linear receiver spreads and 2D grid. Although freight or cargo train energy is considered optimal for surface-wave generation, all local sources are considered during data processing if their wave-propagation direction is aligned or closely aligned with the linear arrays. Data from the 2D grid are used as a quality control measure of this incoming wave energy and wave azimuth. Seismic data records with energy azimuths aligned with one or more of the fixed linear arrays are

Table 1. Active and passive survey geometry.

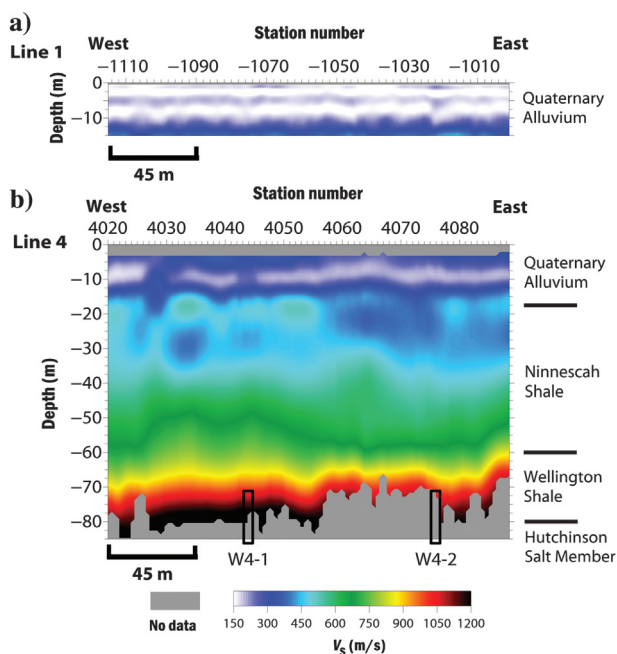| Parameter	Active survey (line 1)	Passive survey (line 4)
Receiver spacing	1.8 m	3 m
Source type	Weight drop	Trains
Source offset	6 m	>1 km
Optimal spread size	42.67 m	84 m

Figure 6. The MASW V_S section with true velocity values from lines 1 and 4 data sets; the geographic location of line 1 is the same as line 4. (a) The 2008 active MASW survey result had a limited depth of investigation compared to (b) the 2017 1D–2D passive MASW survey result.

preferred during selection of a source record for processing that linear array.

Because the wavelengths required to image the entire shale caprock corresponded to 40–80 m depth or approximately 4.5–7.0 Hz, it was critical that high-amplitude coherent energy within this frequency range was recorded to optimize the calculation of dispersion curves and the interpretation of the image. Therefore, source records with dominant, inline, or parallel-wave energy along azimuths corresponding to each line were selected for processing. Frequency-azimuth plots shown in Figure 8a–8c provide examples of potential source records for line 10 with varying signal quality and content. Figure 8a was selected for processing because the highest-amplitude energies are observed with 180° azimuth compared with Figure 8b, which shows recorded omnidirectional source signal (i.e., 0°–360°) between 2.5 and 5.0 Hz. Because Figure 8c displays the recorded source signal at the incorrect azimuth angle (150°), it was also not selected to avoid interference from offline sources.

Dispersion-curve images were also generated for each frequency-azimuth plot (Figure 8d–8f); these provide additional insight about the corresponding dispersion characteristics of the recorded source signal. They are used primarily to determine whether high-amplitude energy corresponds to the fundamental mode and not numerical artifacts such as spectral leakage (Ivanov et al., 2015). Because dispersion-curve images are generated using the 2D square grid array, they are used to guide source selection only, not inversion.

For these line 10 source records (Figure 8), dispersion characteristics exhibit comparable frequency content and phase velocity ranges. Below 3.5 Hz in Figure 8d, the offline source signal is at a minimum with relatively coherent fundamental-mode energy until 17 Hz despite mode energy becoming increasingly attenuated. In Figure 8e, aliasing is more prevalent below 3.5 Hz and the fundamental mode is less discernible between 3.5 and 5.0 Hz due to a potential high-velocity, higher mode in the same frequency range. This may be attributed to the omnidirectional source energies observed in Figure 8b within the same frequency range. The dispersion-curve image in Figure 8f is generally consistent with Figure 8d with strong energy at 3.5 Hz, but the signal is slightly more attenuated between 3.5 and 7.0 Hz in Figure 8f. It is expected that the phase-velocity trend in Figure 8f will also deviate from the true value due to its off-angle source azimuth (i.e., 150°). Overall, these dispersion-curve images provided additional quality control of the recorded source characteristics by revealing attenuated signal and interference from possible higher modes or oblique-angle sources. Based on its 180° directionality (Figure 8a) and higher amplitude and uninterrupted fundamental-mode trend (Figure 8d), source record 1345 was selected for processing line 10.

Source selection was also performed for lines 9 and 11, which were deployed to monitor other areas known to contain dissolution voids. Based on the survey map shown in Figure 4, the orientation of line 9 was 86° and the orientation of line 11 was 74°. High-amplitude energy is observed from approximately 3.5 to 6.5 Hz in each of the three optimal source records selected for lines 9–11 (Figure 9). For line 9, the optimal source record 2746 (Figure 9a) had an 88° azimuth, resulting in a 2° differential between the source azimuth and array orientation. Previously discussed source record 1345 (Figure 9b) was selected for line 10 with a 181° azimuth and 1° differential. Source record selection proved more challenging for line 11, but source record 1092 with a 96° azimuth (Figure 9c)
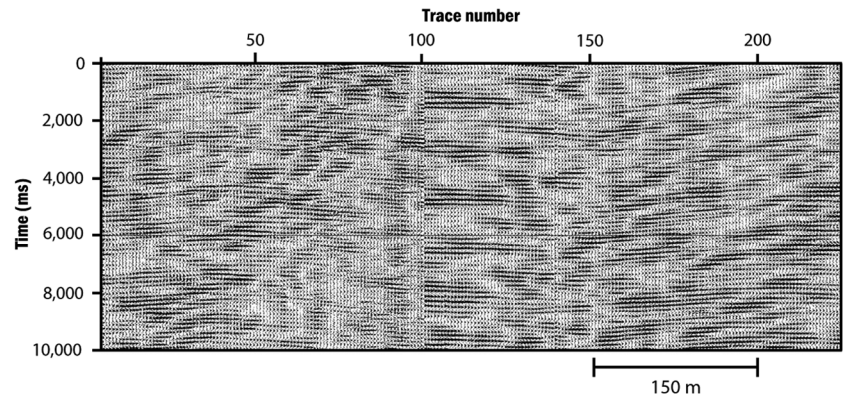

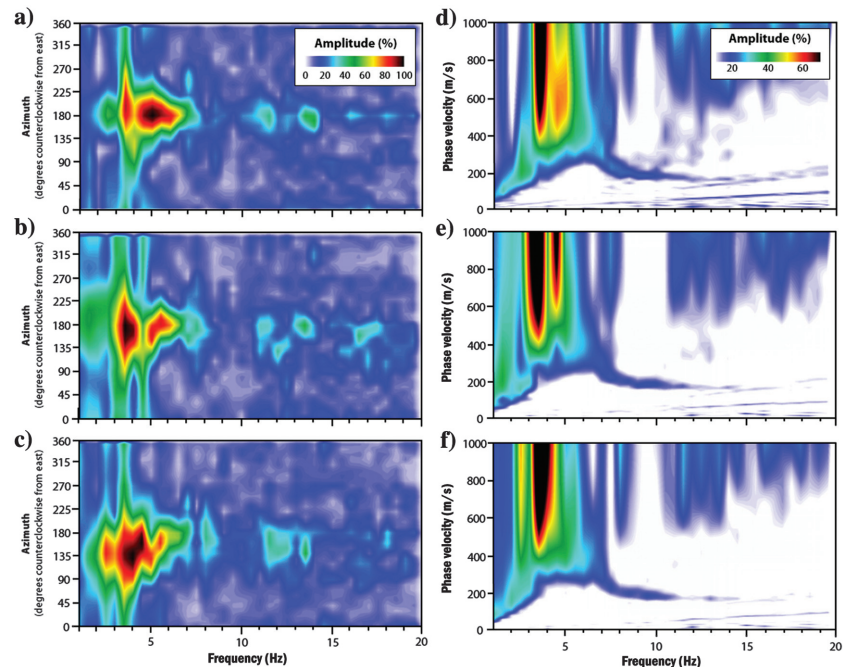Figure 7. Example shot record 2089 displaying signal from an approaching train.

Figure 8. Line 10 frequency-azimuth plot from (a) source record 1345, (b) source record 1087, and (c) source record 1089. Each frequency-azimuth plot has a corresponding dispersion-curve image representing all energy recorded with the full 2D receiver grid. These corresponding dispersion-curve images from (d) source record 1345, (e) source record 1087, and (f) source record 1089 are used to evaluate the quality of the recorded source signal and guide source record selection.

was chosen based on the high-amplitude, continuous energy recorded from approximately 3.5 to 5.0 Hz. This 22° differential between the line orientation (74°) and source azimuth (96°) is easily accounted for following the scale property (Socco and Boiero, 2008) after dispersion-curve inversion using (Park et al., 2004)

$$V_{S,true} = V_{S,app} * \cos \theta. \tag{3}$$

After dispersion-curve inversion, apparent velocities ($V_{S,app}$) are converted to true velocities ($V_{S,true}$), where θ is the degree difference between the array and source azimuths.

After source records were selected for each line, optimal spread sizes were extracted from the fixed receiver spreads (Table 2). In general, high-amplitude fundamental-mode energy was observed from approximately 4.0 to 7.0 Hz for each line (Figure 10) with signal attenuating gradually at higher frequencies. Dispersion curves from line 9 (Figure 10a) and line 10 (Figure 10b) exhibited a dominant fundamental mode with minimal interference from higher modes. However, higher modes were more prevalent on line 11 (Figure 10c, e.g., approximately 1000 m/s at 4 Hz and 800 m/s at 7.0 Hz), which reduced coherency of the fundamental mode above 7.0 Hz.

Subsequently, phase velocities were slightly lower in Figure 10c compared with phase velocities observed on lines 9 and 10 (Figure 10a and 10b, respectively). The fundamental mode did vary across line 10 with western stations having slightly higher phase velocities than eastern stations. Maximum wavelengths recorded at western stations were approximately 132 m ($\lambda_{max} = 627/4.7 = 132$ m) and 201 m ($\lambda_{max} = 724/3.6 = 201$ m), which correspond to maximum depths varying from 66 to 100.5 m (Figure 11b) from west to east ($z_{max} = 132/2 = 66$ m; $z_{max} = 201/2 = 100.5$ m). Nonetheless, picked dispersion curves were inverted to create

Table 2. Survey geometry for linear receiver spreads during passive acquisition.

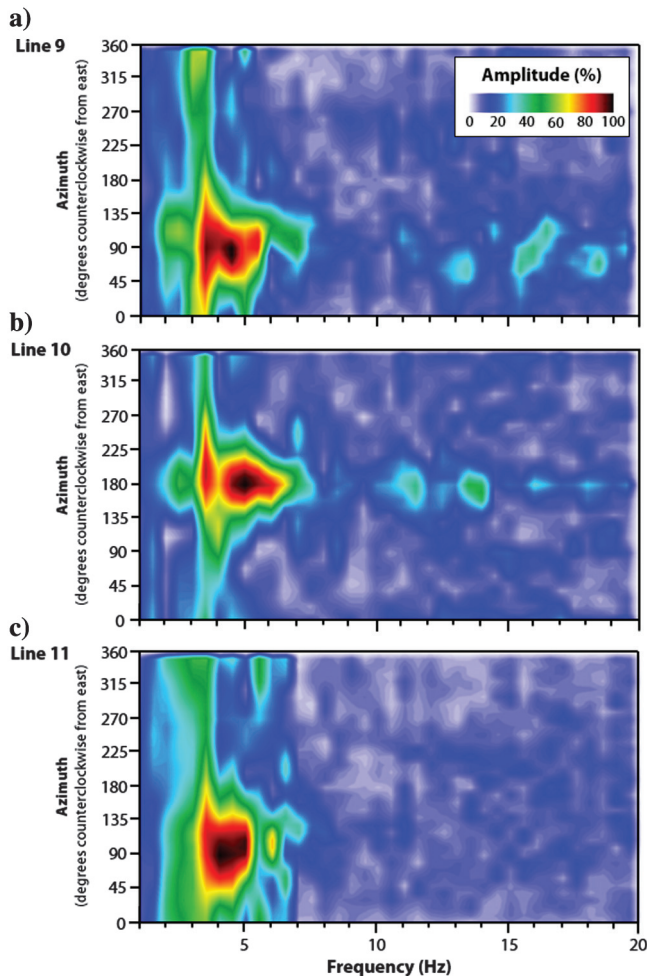| Line	Line azimuth	Source azimuth	Optimal spread size
9	86°	88°	84 m
10	181°	180°	84 m
11	74°	96°	87 m

Figure 9. Source records selected for (a) line 9 with 88° source azimuth, (b) line 10 with 181° source azimuth, and (c) line 11 with 92° source azimuth.
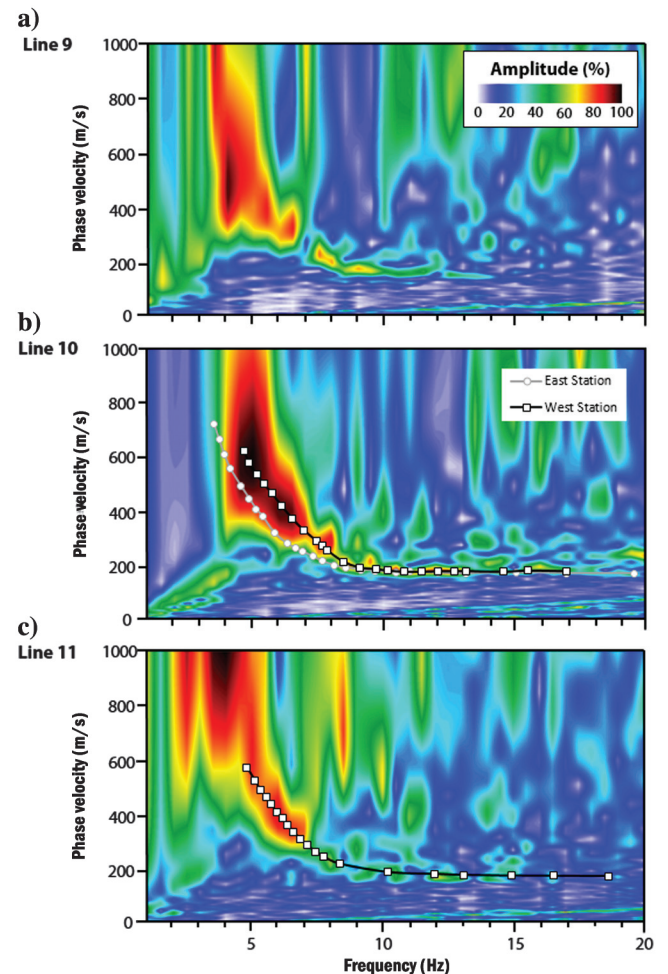

Figure 10. Representative dispersion-curve images from (a) line 9, (b) line 10, and (c) line 11.

MASW V_S sections for each line (Figure 11); equation 3 was used to account for apparent velocity. Lines 9 and 10 had greater depths of investigation than line 11, but the observed bulk-velocity trends were generally consistent with documented geologic materials in this area (Miller et al., 2009). With respect to velocity variations, no anomalously high- or low-velocity features were interpreted on line 9 based on the uniformity observed across the MASW V_S section (Figure 11a). The eastern portion of line 10 (below stations 1040–1055) was noted for reduced V_S below 60 m relative to the western portion of the MASW V_S section (Figure 11b). Finally, the average velocity of the 25–65 m depth interval was lower on line 11 (Figure 11c) than lines 9 and 10. Based on these surveys, the 1D–2D passive MASW method has successfully produced MASW V_S sections with depths greater than 60 m; maximum depth of investigation exceeded 75 m on line 9 and parts of line 10.

DISCUSSION

Some multicomponent processing schemes assume that the ambient noise signal is evenly distributed across all azimuths (Hayashi et al., 2015), whereas some suggest that the source distribution across a 90° angle is sufficient (Asten and Hayashi, 2018). The 1D–2D passive MASW technique presented here uses a single dominant source direction to optimize signal processing. This approach can be used in areas where multiple, dominant inline sources are readily available unlike some of the other passive methods (e.g., SPAC); in this case, each of the trains can be treated as an individual source. In addition, this unidirectional technique limits signal interference because the frequency-azimuth plot selected for processing exhibits incoming source energy that aligns with the seismic array. This focusing increases the S/N and overall quality of the resulting calculations without the risk of near-field effects that can occur with seismic interferometry (Cheng et al., 2015; Zhang et al., 2019). Dispersion curves generated based on their azimuth angle allowed apparent velocity to be corrected to true velocity values, minimizing errors in the final MASW V_S sections. In addition, a unique benefit of the 1D–2D passive MASW method is the ability to measure anisotropy using perpendicular 1D arrays each with optimally aligned sources as demonstrated at this site by Morton et al. (2020).

Key factors that contribute to successful passive processing include recording high S/N and broadband low-frequency content (e.g., 1–20 Hz) of the seismic source signal. Ambient noise produced by trains 1–2 km away has been the best source of seismic signal for this test site, and data acquisition has been customized to allow for optimized processing. Compared with other passive seismic techniques such as HVSR or SPAC, this passive MASW approach only uses a single 30 s record to produce a dispersion image rather than a long continuous record (e.g., 30–60 min). Dispersion-curve images from multiple 30 s source records may be stacked if source records possess the same dominant source azimuth. This can improve the fundamental-mode dispersion trend coherency, but for this study, a single record has proven sufficient. Although this may not be a direct advantage over other passive methods at this test site because the demonstrated acquisition time has been 10–12 h, the acquisition window can be minimized by coordinating acquisition with train schedules. If multiple seismic arrays with different orientations are required, these linear arrays can be deployed in conjunction with the same 2D square grid array. Therefore, surveys of large areas can be designed to fit the needs of

the project while eliminating labor costs associated with operating an active seismic source. By removing the active source from the survey, noise associated with running the active seismic source and potential damage or disturbance to the survey area are no longer factors to consider when working in either urban, rural, or agricultural environments.

Certain considerations need to be taken into account during survey design and data processing when using the 1D–2D passive MASW method. As proven at this test site, it is also advisable that data acquisition extend across several hours to increase the opportunity for successfully recording adequate source energy because the source signal quality and azimuth cannot be controlled by the operator. If a source signal with an azimuth that corresponds to the linear array is not recorded, the resulting apparent velocity values can be adjusted to their true velocity value. From this study at this site, the best fundamental-mode dispersion trends were obtained when the recorded source-to-line azimuth was within 18°, or the apparent velocity is within 5% of the true velocity. Above 5%, interference from offline sources degraded the coherency of the fundamental-mode trend.

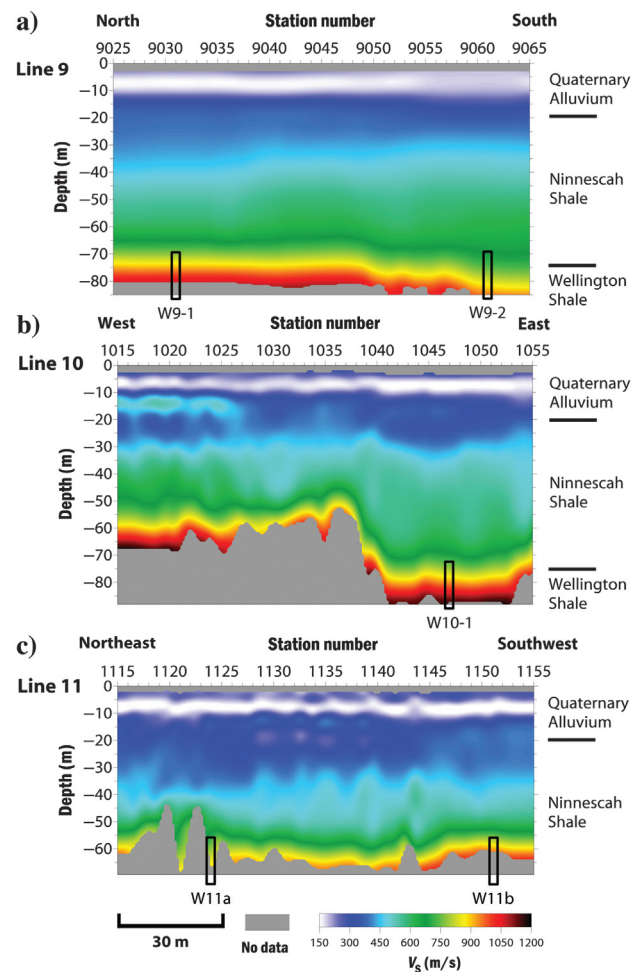Higher-mode interference and lack of fundamental-mode coherency are two of the more common pitfalls encountered with

Figure 11. The MASW V_S section with true velocity values from (a) line 9, (b) line 10, and (c) line 11.

this passive MASW imaging method, both of which are strongly attributed to the quality of the recorded source signal. The near-surface environment is often riddled with local heterogeneities that support the development of higher modes and restrict the imaging of longer fundamental-mode wavelengths with respect to surface-wave sampling at depths greater than 30 m (O'Neill and Matsuoka, 2005). To better identify heterogeneities, Ivanov et al. (2008) recommend decreasing the spread size to increase horizontal resolution at the expense of limiting spread sensitivity to longer wavelengths and consequently limiting the depth of investigation. The high-resolution linear radon transform (HRLRT) method (Luo et al., 2008a, 2008b) has proven successful for isolating the higher and fundamental modes in these passive MASW data (Ivanov et al., 2017b) and active seismic investigations (Ivanov et al., 2017a). If the HRLRT method is unable to discretize different dispersion trends at low frequencies, the dispersion-curve frequency-wavenumber method (Park et al., 2002) can be used to filter higher mode energies by designing a targeted filter zone to reduce unwanted passive surface-wave energy. If performed successfully, higher modes are reduced, allowing the fundamental-mode energy to dominate the filtered frequency range.

Window-selection processing (KGS, 2017; Morton et al., 2019) is another advanced imaging technique that can enhance the continuity of the dispersion trend. The algorithm divides the seismic record into evenly timed sections, and then windows are selected based on a user-assigned root-mean-square criterion; these selected time window(s) are used to generate dispersion-curve images. This method is common in ambient noise processing such as HVSR (Nakamura, 1989), in which the user chooses which signals qualify for optimal processing. In theory, window-selection processing is similar to automatic gain control in that the output amplitudes

are controlled by a multiplier. This multiplier helps to create a more continuous dispersion image as shown in Figure 12. Figure 12a shows subrecord 13064 without window-selection processing, and Figure 12b illustrates how the surface-wave trend images greater continuity with window-selection processing. An awareness of the fundamental-mode trend prior to attempting window-selection processing is necessary due to the potential for overlapping higher modes to interfere with the fundamental mode. This can lead to mode misidentification and an inversion result that inaccurately represents the in situ geologic conditions.

Dispersion-curve stitching is another tool for creating a continuous and coherent energy trend (KGS, 2017). For example, low-frequency signal from subrecord 13064 (Figure 13a) can be combined with higher frequency content from subrecord 13051 (Figure 13b) to produce an enhanced dispersion trend (Figure 13c). These lower and higher frequency dispersion-curve sections are stitched together
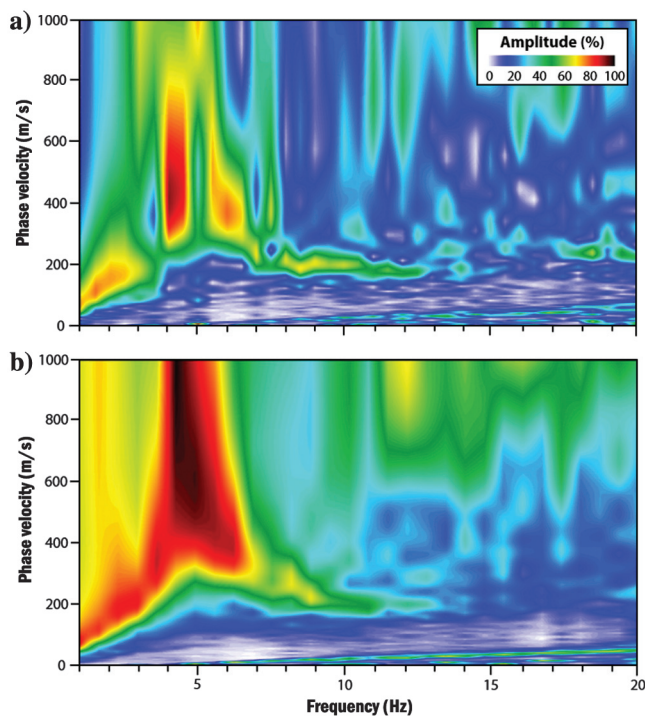

Figure 12. Example dispersion curve from subrecord 13064 (a) before and (b) after window-selection processing was applied on subrecord 1069 during dispersion image generation.
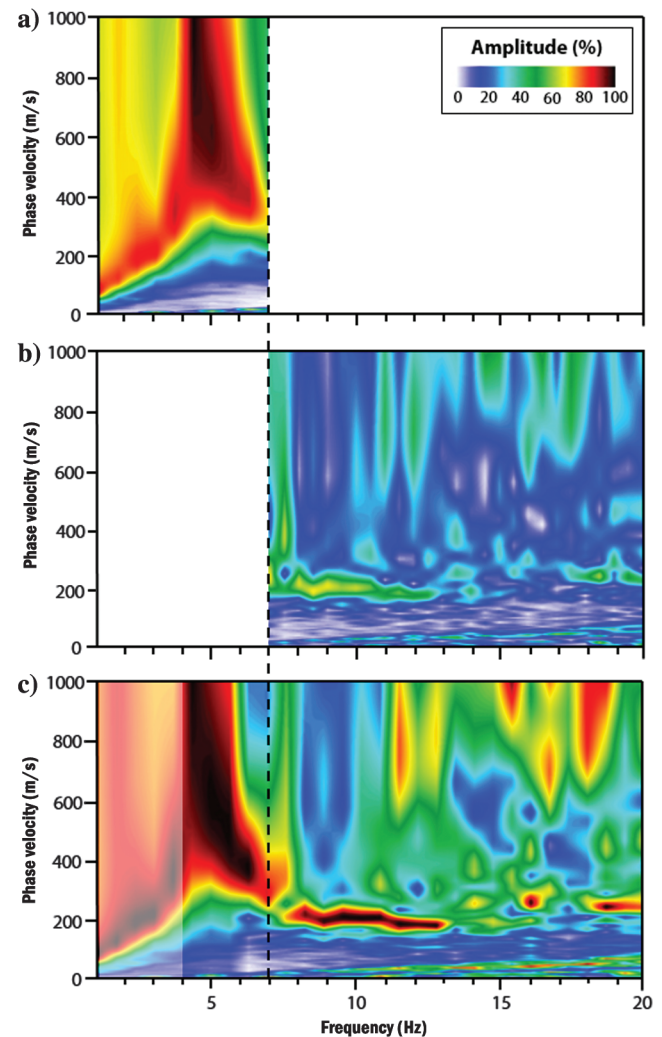

Figure 13. Example of stitched dispersion images in which (a) 1.0–7.0 Hz from subrecord 13064 are processed using the time-window splitting algorithm, (b) 7.0–20.0 Hz from subrecord 13051 are processed with the conventional dispersion imaging algorithm, which are then (c) stitched together to form a combined dispersion-curve image. Dispersion information below 4.0 Hz is likely a numerical artifact and is not considered for data processing.

at a specific frequency value, allowing the user to use frequencies obtained from more than one subrecord. Sections of dispersion images may be stitched together to also combine multiple imaging techniques (e.g., the phase-shift method, HRLRT), different-sized receiver arrays, and source types to enhance the dispersion curve. Once stitched dispersion images are created, high-confidence trends can be picked, and these curves are used as input for 1D inversion processing (Xia et al., 1999).

Given the nature of surface-wave propagation, the amount of averaging in the vertical direction used to produce the final MASW V_S section increases as the depth of investigation increases. For this reason, the deepest inverted layer (half-space layer) may not be part of the velocity interpretation. Therefore, interpretations of these passive data results are performed based on the overall behavior of the measured area (Foti et al., 2014), such as changes in the bulk-velocity structure, rather than fine details (Morton et al., 2020). Shallow velocity inversions can also appear as artifacts of the layered depth model, and are most often related to inversion instabilities generally due to a lack of high-frequency dispersion-curve information that corresponds to the shortest wavelengths associated with these depths; lack of sufficient data can be an issue for any inversion scheme. These inversion features are verified through careful analysis of the picked dispersion trends and experience with the data set and processing procedures.

CONCLUSION

The presented 1D–2D passive MASW method has successfully imaged depths greater than 75 m in which the conventional active MASW method was limited to 14 m at a test site in southcentral Kansas. This method has also proven advantageous because high-amplitude surface-wave source information is easily recorded because high-energy sources (i.e., trains) are a part of the local urban environment. Train energy has proven to generate coherent dispersion curves at this site even though signal coherency can be quite variable from record to record. Conventional mechanical seismic sources such as an accelerated weight drop or sledgehammer source were not necessary to augment for this work, reducing not only the labor costs but also the amount of equipment necessary to be brought to the field site.

Our unique combination of simultaneously using conventional linear array(s) and an additional 2D nested square grid allowed us to use existing source signals and achieve a greater depth of investigation with minimal additional steps. The main contribution of our efforts is the use of this additional 2D receiver grid as an analysis tool and quality control for optimized 1D linear-array passive MASW method acquisition and analysis using only a single source. Other passive methods deploy similar 2D-shaped arrays to different areas to retrieve a velocity profile, whereas the 1D–2D passive MASW method uses a stationary 2D array for optimal processing of multiple 1D arrays. Source records with inline or nearly inline plane-wave propagation only are used for processing to specifically avoid the adverse effects that result from including off-angle source information (i.e., near-field effects). Furthermore, the 1D–2D passive MASW method is more efficient at acquisition and processing for equivalent results obtained using other 2D-array only ambient noise methods because the emphasis is on the use of multiple 1D arrays. A direct benefit of our method can be the ability to measure anisotropy with the availability of favorably available sources.

DATA AND MATERIALS AVAILABILITY

Data associated with this research are confidential and cannot be released.

REFERENCES

Aki, K., 1957, Space and time spectra of stationary stochastic waves with special reference of microtremors: Bulletin of the Earthquake Research Institute, **35**, 415–456.

Akkaya, I., and A. Özvan, 2019, Site characterization in the Van settlement (Eastern Turkey) using surface waves and HVSR microtremor methods: Journal of Applied Geophysics, **160**, 157–170, doi: 10.1016/j.jappgeo.2018.11.009.

Asten, M., T. Dhu, and N. Lam, 2004, Optimised array design for microtremor array studies applied to site classification: Comparison of results with SCPT logs: 13th World Conference on Earthquake Engineering Proceedings, 16.

Asten, M. W., 2006, On bias and noise in passive seismic data from finite circular array data processing using SPAC methods: Geophysics, **71**, no. 6, V153–V162, doi: 10.1190/1.2345054.

Asten, M. W., and K. Hayashi, 2018, Application of the spatial auto-correlation method for shear-wave velocity studies using ambient noise: Surveys in Geophysics, **39**, 633–659, doi: 10.1007/s10712-018-9474-2.

Beroya, M. A. A., A. Aydin, R. Tiglao, and M. Lasala, 2009, Use of microtremor in liquefaction hazard mapping: Engineering Geology, **107**, 140–153, doi: 10.1016/j.enggeo.2009.05.009.

Bodet, L., O. Abraham, and D. Clorennec, 2009, Near-offset effects on Rayleigh-wave dispersion measurements: Physical modeling: Journal of Applied Geophysics, **68**, 95–103, doi: 10.1016/j.jappgeo.2009.02.012.

Bonnefoy-Claudet, S., C. Cornou, P.-Y. Bard, F. Cotton, P. Moczo, J. Kristek, and D. Fäh, 2006, H/V ratio: A tool for site effects evaluation. Results from 1-D noise simulations: Geophysical Journal International, **167**, 827–837, doi: 10.1111/j.1365-246X.2006.03154.x.

Capon, J., 1969, High-resolution frequency-wavenumber spectrum analysis: Proceedings of the IEEE, **57**, 1408–1418, doi: 10.1109/PROC.1969.7278.

Carniel, R., P. Malisan, F. Barazza, and S. Grimaz, 2008, Improvement of HVSR technique by wavelet analysis: Soil Dynamics and Earthquake Engineering, **28**, 321–327, doi: 10.1016/j.soildyn.2007.06.006.

Chavéz-Garcia, F. J., M. Rodriguez, and W. R. Stephenson, 2006, Subsoil structure using SPAC measurements along a line: Bulletin of the Seismological Society of America, **96**, 729–736.

Cheng, F., J. Xia, Y. Luo, Z. Xu, L. Wang, C. Shen, R. Liu, Y. Pan, B. Mi, and Y. Hu, 2016, Multichannel analysis of passive surface waves based on crosscorrelations: Geophysics, **81**, no. 5, EN57–EN66, doi: 10.1190/geo2015-0505.1.

Cheng, F., J. Xia, Z. Xu, Y. Hu, and B. Mi, 2017, Frequency-wavenumber (FK)-based data selection in high-frequency passive surface wave survey: Surveys in Geophysics, **39**, 661–682, doi: 10.1007/s10712-018-9473-3.

Cheng, F., J. Xia, Y. Xu, Z. Xu, and Y. Pan, 2015, A new passive seismic method based on seismic interferometry and multichannel analysis of surface waves: Journal of Applied Geophysics, **117**, 126–135, doi: 10.1016/j.jappgeo.2015.04.005.

Claprood, M., and M. W. Asten, 2007, Combined use of SPAC, FK, and HVSR microtremor survey methods for site hazard study over the 2D Tamar Valley, Launceston, Tasmania: 19th Geophysical Conference, ASEG, 1–4.

Cornou, C., S. Michel, E. Pathier, G. Menard, M. Collombet, and P.-Y. Bard, 2011, Use of subsidence rate as proxy for resonance period: 4th IASPEI IAEE International Symposium Proceedings, 1–10.

Cox, B. R., and A. N. Beekman, 2011, Intramethod variability in ReMi dispersion measurements and Vs estimates at shallow bedrock sites: Journal of Geotechnical and Geoenvironmental Engineering, **137**, 354–362, doi: 10.1061/(ASCE)GT.1943-5606.0000436.

Curtis, A., P. Gerstoft, H. Sato, R. Snieder, and K. Wapenaar, 2006, Seismic interferometry — Turning noise into signal: The Leading Edge, **25**, 1082–1092, doi: 10.1190/1.2349814.

Dal Moro, G., 2015, Horizontal-to-vertical spectral ratio, *in* G. Dal Moro, ed., Surface wave analysis for near surface applications: Elsevier, 65–85.

Delgado, J., C. L. Casado, A. Estevez, J. Giner, A. Cuenca, and S. Molina, 2000a, Mapping soft soils in the Segura river valley (SE Spain): A case study of microtremors as an exploration tool: Journal of Applied Geophysics, **45**, 19–32, doi: 10.1016/S0926-9851(00)00016-1.

Delgado, J., C. L. Casado, A. Estevez, J. Giner, A. Cuenca, and S. Molina, 2000b, Microtremors as a geophysical exploration tool: Applications and limitations: Pure and Applied Geophysics, **157**, 1445–1462, doi: 10.1007/PL00001128.

Di Giulio, G., C. Cornou, M. Ohrnberger, M. Wathelet, and A. Rovelli, 2006, Deriving wavefield characteristics and shear-velocity profiles from two-dimensional small-aperture arrays analysis of ambient vibrations in a small-size alluvial basin, Colfiorito, Italy: Bulletin of the Seismological Society of America, **96**, 1915–1933, doi: 10.1785/0120060119.

Dobecki, T. L., and S. B. Upchurch, 2006, Geophysical applications to detect sinkholes and ground subsidence: The Leading Edge, **25**, 336–341, doi: 10.1190/1.2184102.

Foti, S., F. Hollender, F. Garofalo, D. Albarello, M. Asten, P.-Y. Bard, C. Comina, C. Cornou, B. Cox, G. Di Giulio, T. Forbriger, K. Hayashi, E. Lunedei, A. Martin, D. Mercerat, M. Ohrnberger, V. Poggi, F. Renalier, D. Silicia, and V. Socco, 2018, Guidelines for the good practice of surface wave analysis: A product of the InterPACIFIC project: Bulletin of Earthquake Engineering, **16**, 2367–2420, doi: 10.1007/s10518-017-0206-7.

Foti, S., C. G. Lai, G. J. Rix, and C. Strobbia, 2014, Surface wave methods for near-surface site characterization: CRC Press.

Garofalo, F., S. Foti, F. Hollender, P. Y. Bard, C. Cornou, B. R. Cox, M. Ohrnberger, D. Sicilia, M. Asten, G. Di Giulio, T. Forbriger, B. Guillier, K. Hayashi, A. Martin, S. Matsushima, D. Mercerat, V. Poggi, and H. Yamanaka, 2016, InterPACIFIC project: Comparison of invasive and non-invasive methods for seismic site characterization — Part 1: Intracomparison of surface wave methods: Soil Dynamics and Earthquake Engineering, **82**, 222–240, doi: 10.1016/j.soildyn.2015.12.010.

Halliday, D., and A. Curtis, 2008, Seismic interferometry, surface waves and source distribution: Geophysical Journal International, **175**, 1067–1087, doi: 10.1111/j.1365-246X.2008.03918.x.

Hayashi, K., M. Craig, T. Kita, and T. Inazaki, 2015, CMP spatial autocorrelation analysis of multichannel passive surface-wave data: 85th Annual International Meeting, SEG, Expanded Abstracts, 2200–2204, doi: 10.1190/segam2015-5913708.1.

Henstridge, J. D., 1979, A signal processing method for circular arrays: Geophysics, **44**, 179–184, doi: 10.1190/1.1440959.

Ivanov, J., B. Leitner, W. Shefchik, J. T. Schwenk, and S. Peterie, 2013, Evaluating hazards at salt cavern sites using multichannel analysis of surface waves: The Leading Edge, **32**, 298–305, doi: 10.1190/tle32030298.1.

Ivanov, J., R. D. Miller, D. Feigenbaum, S. L. C. Morton, S. L. Peterie, and J. B. Dunbar, 2017a, Revisiting levees in southern Texas using Love-wave multichannel analysis of surface waves with the high-resolution linear Radon transform: Interpretation, **5**, no. 3, T287–T298, doi: 10.1190/INT-2016-0044.1.

Ivanov, J., R. D. Miller, D. Z. Feigenbaum, and J. T. Schwenk, 2017b, Benefits of using the high-resolution linear radon transform (HRLRT) with the multi-channel analysis of surface waves (MASW) method: 87th Annual International Meeting, SEG, Expanded Abstracts, 2647–2653, doi: 10.1190/segam2017-17793766.1.

Ivanov, J., R. Miller, P. Lacombe, C. D. Johnson, and J. W. Lane Jr., 2006, Delineating a shallow fault zone and dipping bedrock strata using multichannel analysis of surface waves with a land streamer: Geophysics, **71**, no. 5, A39–A42, doi: 10.1190/1.2227521.

Ivanov, J., R. D. Miller, S. Morton, and S. Peterie, 2015, Dispersion-curve imaging considerations when using multichannel analysis of surface waves (MASW) method: Symposium on the Application of Geophysics to Engineering and Environmental Problems, 556–566.

Ivanov, J., R. D. Miller, S. Peterie, C. Zeng, J. Xia, and T. Schwenk, 2011, Multi-channel analysis of surface waves (MASW) of models with high shear-wave velocity contrast: 81st Annual International Meeting, SEG, Expanded Abstracts, 1384–1390, doi: 10.1190/1.3627461.

Ivanov, J., R. Miller, and G. Tsoflias, 2008, Some practical aspects of MASW analysis and processing: Symposium on Applications in Geophysics for Environmental and Engineering Problems Proceedings, 1186–1198.

Kansas Geological Survey (KGS), 2017, SurfSeis 6 user's manual: Kansas Geological Survey, 19.

Karastathis, V. K., A. Ganas, J. Makris, J. Papoulia, P. Dafnis, E. Gerolymatou, and G. Drakatos, 2007, The application of shallow seismic techniques in the study of active faults: The Atalanti normal fault, central Greece: Journal of Applied Geophysics, **62**, 215–233, doi: 10.1016/j.jappgeo.2006.11.004.

Kind, F., D. Fäh, and D. Giardini, 2004, Array measurements of S-wave velocities from ambient vibrations: Geophysical Journal International, **160**, 114–126, doi: 10.1111/j.1365-246X.2005.02331.x.

Kita, T., K. Hayashi, and H. Bingol, 2011, The development of a 2-dimensional microtremor survey method based on SPAC method using sequential linear arrays: Symposium on Applications in Geophysics for Environmental and Engineering Problems Proceedings, 115–120.

Le Feuvre, M., A. Joubert, D. Leparoux, and P. Côte, 2015, Passive multi-channel analysis of surface waves with cross-correlations and beamforming. Application to a sea dike: Journal of Applied Geophysics, **114**, 36–51, doi: 10.1016/j.jappgeo.2014.12.014.

Leitner, B., R. Miller, and J. Ivanov, 2011, Optimal spread design for passive MASW: 17th European Meeting of Environmental and Engineering Geophysics Proceedings, doi: https://doi.org/10.3997/2214-4609.20144379.

Leitner, B., R. Miller, and J. Ivanov, 2012, Orientated passive MASW — Influence of source energy from multiple directions: 18th European Meeting of Environmental and Engineering Geophysics Proceedings, doi: https://doi.org/10.3997/2214-4609.20143456.

Liu, L., Q.-F. Chen, W. Wang, and E. Rohrbach, 2014, Ambient noise as the new source for urban engineering seismology and earthquake engineering: A case study from Beijing metropolitan area: Earthquake Science, **27**, 89–100, doi: 10.1007/s11589-013-0052-x.

Louie, J. N., 2001, Faster, better: Shear-wave velocity to 100 meters depth from refraction microtremor arrays: Bulletin of Seismological Society of America, **91**, 347–364, doi: 10.1785/0120000098.

Luo, S., Y. Luo, L. Zhu, and Y. Xu, 2016, On the reliability and limitations of the SPAC method with a directional wavefield: Journal of Applied Geophysics, **126**, 172–182, doi: 10.1016/j.jappgeo.2016.01.023.

Luo, Y., Y. Xu, Q. Liu, and J. Xia, 2008a, Rayleigh-wave dispersive energy imaging and mode separating by high-resolution linear radon transform: The Leading Edge, **27**, 1536–1542, doi: 10.1190/1.3011026.

Luo, Y. H., J. H. Xia, R. D. Miller, Y. X. Xu, J. P. Liu, and Q. S. Liu, 2008b, Rayleigh-wave dispersive energy imaging using a high-resolution linear radon transform: Pure and Applied Geophysics, **165**, 903–922, doi: 10.1007/s00024-008-0338-4.

Miller, R. D., J. Ivanov, S. D. Sloan, S. Walters, B. Leitner, A. Rech, B. Wedel, A. R. Wedel, J. M. Anderson, O. M. Metheny, and J. C. Schwarzer, 2009, Shear-wave seismic study above Vigindustries, Inc. legacy salt jugs in Hutchinson, Kansas: Kansas Geological Survey Open-file Report 2009-3, 42.

Miller, R. D., J. Xia, C. Park, and J. Ivanov, 1999, Multichannel analysis of surface waves to map bedrock: The Leading Edge, **18**, 1392–1396, doi: 10.1190/1.1438226.

Molnar, S., J. F. Cassidy, S. Castellaro, C. Cornou, H. Crow, J. A. Hunter, S. Matsushima, F. J. Sanchez-Sesma, and A. Yong, 2018, Application of microtremor horizontal-to-vertical spectral ratio (MHVSR) analysis for site characterization: State-of-the-art: Surveys in Geophysics, **39**, 613–631, doi: 10.1007/s10712-018-9464-4.

Moon, S.-W., K. Hayashi, and T. Ku, 2017, Estimating spatial variations in bedrock depth and weathering degree in decomposed granite from surface wave: Journal of Geotechnical and Geoenvironmental Engineering, **143**, 04017020, doi: 10.1061/(ASCE)GT.1943-5606.0001679.

Morton, S. L., J. Ivanov, and R. D. Miller, 2019, Selective-window processing for optimized surface wave imaging of passive data: 89th Annual International Meeting, SEG, Expanded Abstracts, 5035–5039, doi: 10.1190/segam2019-3216790.1.

Morton, S. L., R. D. Miller, J. Ivanov, S. L. Peterie, and R. L. Parsons, 2020, Time-lapse monitoring of stress-field variations within the Ninnescah Shale and Wellington Formation in Kansas: The Leading Edge, **39**, 318–323, doi: 10.1190/tle39050318.1.

Nakamura, Y., 1989, A method for dynamic characteristics estimation of subsurface using microtremor on the ground surface: Quarterly Report of the Railway Technical Research Institute, **30**, 25–33.

Nakata, N., 2016, Near-surface S-wave velocities estimated from traffic-induced Love waves using seismic interferometry with double beamforming: Interpretation, **4**, no. 4, SQ23–SQ31, doi: 10.1190/INT-2016-0013.1.

Nogoshi, M., and T. Igarashi, 1970, On the propagation characteristics of microtremors (in Japanese with English abstract): Journal of the Seismological Society of Japan, **23**, 264–280.

Nogoshi, M., and T. Igarashi, 1971, On the amplitude characteristics of microtremor — Part 2: Journal of the Seismological Society of Japan, **24**, 26–40.

O'Neill, A., and T. Matsuoka, 2005, Dominant higher surface-wave modes and possible inversion pitfalls: Journal and Environmental and Engineering Geophysics, **10**, 185–201, doi: 10.2113/JEEG10.2.185.

Park, C., R. D. Miller, D. Laflen, N. Cabrillo, J. Ivanov, and B. Bennett, 2004, Imaging dispersion curves of passive surface waves: 74th Annual International Meeting, SEG, Expanded Abstracts, 1357–1360, doi: 10.1190/1.1851112.

Park, C. B., 2008, Imaging dispersion of passive surface waves with active scheme: Symposium on the Application of Geophysics to Engineering and Environmental Problems Proceedings, 1218–1225.

Park, C. B., and R. D. Miller, 2005, Multichannel analysis of passive surface waves — Modeling and processing schemes: ASCE/Geo-Institute Geo-Frontiers Proceedings, 23–26.

Park, C. B., and R. D. Miller, 2008, Roadside passive multichannel analysis of surface waves (MASW): Journal of Environmental and Engineering Geophysics, **13**, 1–11, doi: 10.2113/JEEG13.1.1.

Park, C. B., R. D. Miller, and J. Ivanov, 2002, Filtering surface waves: Symposium on the Applications of Geophysics to Engineering and Environmental Problems Proceedings, SEI9–SEI9.

Park, C. B., R. D. Miller, and J. Xia, 1998, Imaging dispersion curves of surface waves on multi-channel record: 68th Annual International Meeting, SEG, Expanded Abstracts, 874–877, doi: 10.1190/1.1820161.

Park, C. B., R. D. Miller, J. H. Xia, and J. Ivanov, 2007, Multichannel analysis of surface waves (MASW) — Active and passive methods: The Leading Edge, **26**, 60–64, doi: 10.1190/1.2431832.

Parker, E. H. J., and R. B. Hawman, 2012, Multi-channel analysis of surface waves (MASW) in karst terrain, Southwest Georgia: Implications for detecting anomalous features and fracture zones: Journal and Environmental and Engineering Geophysics, **17**, 129–150, doi: 10.2113/JEEG17.3.129.

Richart, F. E., J. R. Hall, and R. D. Woods, 1970, Vibrations of soils and foundations: Prentice Hall Inc.

Rix, G. J., and A. E. Leipski, 1991, Accuracy and resolution of surface wave inversion: American Society of Civil Engineering Geotechnical Special Publication no. 28, 17–23.

Rosenblad, B. L., and R. Goetz, 2010, Study of the H/V spectral ratio method for determining average shear wave velocities in the Mississippi embayment: Engineering Geology, **112**, 13–20, doi: 10.1016/j.enggeo.2010.01.006.

Rosenblad, B. L., and J. Li, 2009, Comparative study of refraction microtremor (ReMi) and active source methods for developing low-frequency surface wave dispersion curves: Journal of Environmental and Engineering Geophysics, **14**, 101–113, doi: 10.2113/JEEG14.3.101.

Rost, S., and C. Thomas, 2002, Array seismology: Methods and applications: Reviews of Geophysics, **40**, 1–27, doi: 10.1029/2000RG000100.

Schuster, G. T., 2001, Theory of daylight/interferometric imaging — Tutorial: 63rd Annual International Conference and Exhibition, EAGE, Extended Abstracts, A32, doi: 10.3997/2214-4609-pdb.15.A-32.

Schuster, G. T., 2009, Seismic interferometry: Cambridge University Press.

Sheriff, R. E., and L. P. Geldart, 1995, Exploration seismology, 2nd ed.: Cambridge University Press.

Silahtar, A., M. Z. Kanbur, and G. Beyhan, 2020, Analysis of seismic site characterization of the Isparta basin (southwestern Turkey) using passive surface-wave method (ReMiTM) and borehole data: Journal of Earth System Science, **129**, 67, doi: 10.1007/s12040-019-1310-7.

Sloan, S. D., R. D. Miller, J. Ivanov, and S. Walters, 2009, Shear-wave velocity as an indicator of increased stress and failure potential associated with dissolution mining voids: Symposium on the Application of Geophysics to Engineering and Environmental Problems Proceedings, 363–372.

Snieder, R., 2004, Extracting the Green's function from the correlation of coda waves: A derivation based on stationary phase: Physical Review E, **69**, 046610, doi: 10.1103/PhysRevE.69.046610.

Socco, L. V., and D. Boiero, 2008, Improved Monte Carlo inversion of surface wave data: Geophysical Prospecting, **56**, 357–371, doi: 10.1111/j.1365-2478.2007.00678.x.

Song, Y.-Y., J. P. Castagna, R. A. Black, and R. W. Knapp, 1989, Sensitivity of near-surface shear-wave velocity determination from Rayleigh and Love waves: 59th Annual International Meeting, SEG, Expanded Abstracts, 509–512, doi: 10.1190/1.1889669.

Walters, R. F., 1978, Land subsidence in central Kansas related to salt dissolution: Kansas Geological Survey Bulletin, **214**, 1–32.

Wapenaar, K., D. Draganov, R. Snieder, X. Campman, and A. Verdel, 2010, Tutorial on seismic interferometry — Part 1: Basic principles and applications: Geophysics, **75**, no. 5, 75A195–75A209, doi: 10.1190/1.3457445.

Wathelet, M., D. Jongmans, M. Ohrnberger, and S. Bonnefoy-Claudet, 2008, Array performances for ambient vibrations on a shallow structure and consequences over Vs inversion: Journal of Seismology, **12**, 1–19, doi: 10.1007/s10950-007-9067-x.

Watney, W. L., S. E. Nissen, S. Bhattacharya, and D. Young, 2003, Evaluation of the role of evaporite karst in the Hutchinson, Kansas gas explosions, January 17 and 18, 2001: Oklahoma Geological Survey Circular, **109**, 119–147.

Xia, J., R. D. Miller, and C. Park, 1999, Estimation of near-surface shear-wave velocity by inversion of Rayleigh waves: Geophysics, **64**, 691–700, doi: 10.1190/1.1444578.

Xu, C., and S. D. Butt, 2006, Evaluation of MASW techniques to image steeply dipping cavities in laterally inhomogeneous terrain: Journal of Applied Geophysics, **59**, 106–116, doi: 10.1016/j.jappgeo.2005.08.003.

Zhang, Y., Y. E. Li, H. Zhang, and T. Ku, 2019, Near-surface site investigation by seismic interferometry using urban traffic noise in Singapore: Geophysics, **84**, no. 2, B169–B180, doi: 10.1190/geo2017-0798.1.

Zhao, Y., and J. W. Rector, 2010, Using seismic surface waves generated by motor vehicles to find voids: Field results: 80th Annual International Meeting, SEG, Expanded Abstracts, 2029–2033, doi: 10.1190/1.3513243.

Biographies and photographs of the authors are not available.